Microtubule-associated IQD9 orchestrates cellulose patterning in seed mucilage

Bo Yang[1] (iD)**, Gina Stamm**[2]**, Katharina Bürstenbinder**[2] (iD) **and Cătălin Voiniciuc**[1,3] (iD)

[1]Independent Junior Research Group–Designer Glycans, Leibniz Institute of Plant Biochemistry, 06120, Halle (Saale), Germany; [2]Department of Molecular Signal Processing, Leibniz Institute of Plant Biochemistry, 06120, Halle (Saale), Germany; [3]Horticultural Sciences Department, University of Florida, Gainesville, FL 32611, USA

Authors for correspondence:
Katharina Bürstenbinder
Email: Katharina.Buerstenbinder@ipb-halle.de

Cătălin Voiniciuc
Email: Catalin.Voiniciuc@ipb-halle.de

Summary

- Arabidopsis seeds release large capsules of mucilaginous polysaccharides, which are shaped by an intricate network of cellulosic microfibrils. Cellulose synthase complexes are guided by the microtubule cytoskeleton, but it is unclear which proteins mediate this process in the seed coat epidermis.
- Using reverse genetics, we identified *IQ67 DOMAIN 9* (*IQD9*) and *KINESIN LIGHT CHAIN-RELATED 1* (*KLCR1*) as two highly expressed genes during seed development and comprehensively characterized their roles in cell wall polysaccharide biosynthesis.
- Mutations in *IQD9* as well as in *KLCR1* lead to compact mucilage capsules with aberrant cellulose distribution, which can be rescued by transgene complementation. IQD9 physically interacts with KLCR1 and localizes to cortical microtubules (MTs) to maintain their organization in seed coat epidermal (SCE) cells. IQD9 as well as a previously identified TONNEAU1 (TON1) RECRUITING MOTIF 4 (TRM4) protein act to maintain cellulose synthase velocity.
- Our results demonstrate that IQD9, KLCR1 and TRM4 are MT-associated proteins that are required for seed mucilage architecture. This study provides the first direct evidence that members of the IQD, KLCR and TRM families have overlapping roles in cell wall biosynthesis. Therefore, SCE cells provide an attractive system to further decipher the complex genetic regulation of polarized cellulose deposition.

Introduction

The seed coat epidermal (SCE) cells of some angiosperms, including the model plant *Arabidopsis thaliana*, synthesize large amounts of hydrophilic polysaccharides (North *et al.*, 2014; Voiniciuc *et al.*, 2015c; Šola *et al.*, 2019). Although the mucilage capsules that rapidly surround Arabidopsis seeds upon hydration are pectin-rich, they can be regarded as specialized secondary cell walls because they also contain hemicelluloses that are typical of woody tissues (Voiniciuc *et al.*, 2015c). Substituted xylans and heteromannans maintain the attachment of mucilaginous pectin to the seed surface and the organization of ray-like cellulose microfibrils (Yu *et al.*, 2014; Voiniciuc *et al.*,2015a,b; Hu *et al.*, 2016; Ralet *et al.*, 2016). Upon imbibition of a dry seed, expanding mucilage ruptures the outer primary cell wall to release a two-layered gelatinous capsule that can be visualized by ruthenium red (RR), a pectin-binding dye. Cellulosic rays extend from the top of each SCE cell to intertwine and anchor the inner, adherent mucilage layer to the seed surface (Harpaz-Saad *et al.*, 2011; Mendu *et al.*, 2011; Sullivan *et al.*, 2011). However, the genetic factors that modulate the deposition of highly ordered cellulosic structures in seed mucilage remain largely unknown.

The current dogma is that plant crystalline microfibrils are produced by rosette-shaped cellulose synthase (CESA) complexes

(CSCs) composed of at least three different CESA isoforms and a growing number of interacting proteins (Polko & Kieber, 2019). In Arabidopsis SCE cells, mutations in *CESA3* and *CESA5* have been shown to affect the deposition of cellulose in mucilage pockets. Loss-of-function *cesa5* mutants have a nearly complete loss of adherent mucilage due to reduced cellulose production (Harpaz-Saad *et al.*, 2011; Mendu *et al.*, 2011; Sullivan *et al.*, 2011), while *cesa3* missense mutants lead to milder alterations of mucilage adherence and cellulose organization (Griffiths *et al.*, 2015). Several accessory proteins are also known to influence mucilage cellulose synthesis. COBRA-LIKE2 (COBL2) contains a glycosyl-phosphatidylinositol (GPI) anchor and facilitates the assembly of crystalline cellulose by CESA5 (Ben-Tov *et al.*, 2015), while FEI2 (meaning 'fat' in Chinese) and SALT-OVERLY SENSITIVE5 (SOS5) mediate pectin adherence to cellulosic rays via an independent mechanism (Griffiths *et al.*, 2014, 2016; Ben-Tov *et al.*, 2018). CSC assembly and trafficking are maintained by STELLOs (Greek for 'to send'; Zhang *et al.*, 2016), and negatively regulated by SHOU4 ('thin' in Chinese; Polko *et al.*, 2018), identified via a screen for *fei2* suppressors.

Cortical microtubules (MTs) can orient cellulose microfibril deposition by positioning the delivery of CSCs to the plasma membrane (PM) and guiding their subsequent trajectories (Paredez *et al.*, 2006; Gutierrez *et al.*, 2009; Bringmann *et al.*, 2012a).

MT-associated proteins, which shape the cytoskeleton in response to environmental or developmental signals (Lloyd & Hussey, 2001; Sedbrook & Kaloriti, 2008), can influence the organization of mucilage polysaccharides. A temperature-sensitive point mutation in *MICROTUBULE ORGANIZATION 1* (*MOR1*) significantly reduced mucilage release at 29°C (McFarlane *et al.*, 2008). A second MT-associated protein, TONNEAU1 (TON1) RECRUITING MOTIF 4 (TRM4), was recently found to organize cortical arrays and cellulose distribution (Yang *et al.*, 2019). The *trm4* seed mucilage capsules are compact and have shorter cellulosic rays compared to the wild-type (WT), without altering pectin adherence. Arabidopsis CESAs circle around the cytoplasmic column of SCE cells to polarly deposit cellulose microfibrils in mucilage pockets (Griffiths *et al.*, 2015), but the network of proteins that guide CESAs in SCE cells remains unclear.

Plant-specific IQ67 DOMAIN (IQD) proteins associate with MTs and have scaffold-like properties (Bürstenbinder *et al.*, 2017). Their eponymous IQ67 domain contains 67 amino acids with calmodulin-recruiting motifs (Abel *et al.*, 2005), which could be involved in Ca^{2+} signaling integration (Kölling *et al.*, 2019). Since multiple Arabidopsis IQDs control cell shape and size (Bürstenbinder *et al.*, 2017; Liang *et al.*, 2018; Mitra *et al.*, 2019), they are hypothesized to support cell wall deposition. Certain IQDs interact with KINESIN LIGHT CHAIN-RELATEDs (KLCRs; Bürstenbinder *et al.*, 2013; Zang *et al.*, 2021) proteins. KLCRs are also known as CELLULOSE SYNTHASE-MICROTUBULE UNCOUPLING (CMU) and stabilize MTs at the PM during cellulose synthesis (Liu *et al.*, 2016). However, direct evidence for how IQDs influence the biosynthesis of cell wall polysaccharides has been lacking.

In this study, we identified IQD9 and KLCR1 as two additional players that maintain MT organization and the deposition of ray-like cellulosic microfibrils in SCE cells. In the absence of *IQD9* or *KLCR1*, mutant seeds released compact mucilage capsules due to aberrant deposition of cellulose microfibrils, as previously observed for *trm4* lines. IQD9 physically interacted *in vivo* with KLCR1 and formed filamentous arrays. Live-cell imaging showed that IQD9 and KLCR1 are localized in a circular pattern during mucilage biosynthesis, which is reminiscent of CSC trajectories. Both *iqd9* and *trm4* mutants displayed slower CESA3 particles in SCE cells, indicating that these MT-associated proteins guide cellulose deposition. IQD, KLCR and TRM proteins therefore have overlapping roles in cell wall biosynthesis.

Materials and Methods

Plant materials and growth conditions

Arabidopsis thaliana Col-0 (WT) and T-DNA insertion mutants (Supporting Information Table S1) analyzed in this study were obtained from the Nottingham Arabidopsis Stock Centre, unless otherwise noted. The *proUBQ:RFP-TUB6* in Col-0 (Ambrose *et al.*, 2011), *proCESA3:GFP-CESA3* in *je5* mutant (Desprez *et al.*, 2007) and *pKLCR1:KLCR1-GFP* in *klcr1-1* (Zang *et al.*, 2021) transgenic plants have been described previously.

Arabidopsis plants were grown in a phytochamber with constant light (100–120 µmol m^{-2} s^{-1}), 22°C and 60% humidity. *Nicotiana benthamiana* plants were grown in a glasshouse (16 h : 8 h, light : dark) at 22–24°C.

Arabidopsis transcriptional analyses

Total RNA was isolated from 10-d-old seedlings using TRI Reagent (Sigma Aldrich, Darmstadt, Germany), according to its manual. The cDNA was prepared from 4 µg of RNA using RevertAid reverse Transcriptase (Thermo Fisher Scientific, Waltham, MA, USA), and reverse transcription PCR (RT-PCR) was performed using the primers listed in Table S2. *ACTIN2* served as a housekeeping gene, and WT genomic DNA was included as a control.

For β-glucuronidase (GUS) reporter staining, sample tissues (seedlings, flower buds, siliques) were fixed in 80% (v/v) ice-cold acetone for 30 min and incubated for 4 h to overnight in GUS staining solution (50 mM sodium phosphate, pH 7.2, 0.5 mM $K_3Fe(CN)_6$, 0.5 mM $K_4Fe(CN)_6$, 2 mM 5-bromo-4-chloro-3-indolyl-β-glucuronic acid, 10 mM EDTA) at 37°C. Images were acquired using a Zeiss Axioplan 2 microscope or a Nikon SMZ 1000. For GUS staining of Arabidopsis seeds, siliques of different ages were opened with forceps at the replum. Seeds were collected with a small spoon and transferred to a 1.5 ml tube with staining solution. Before differential interference contrast (DIC) microscopy, staining solution was removed and samples were mounted in chloralhydrate.

Plasmid construction and plant transformation

Primers used for plasmid construction are listed in Table S2. *Promoter*:*GFP-GUS* constructs were generated by integrating 1.4 kb of the *IQD9* or *IQD10* promoter into pBGWFS7 (Karimi *et al.*, 2002). The *pIQD9:IQD9-GFP* transgene was assembled using full-length genomic DNA (from *c.* 1.5 kb upstream of ATG up to, but excluding, the *IQD9* stop codon) into pB7FWG0 vector. The constructs were stably transformed into Arabidopsis WT plants (for *pIQD:GFP-GUS*) or *iqd9 iqd10* double mutant (for *pIQD9:IQD9-GFP*) respectively via *Agrobacterium*-mediated floral dip transformation. The *p35S:IQD9-GFP*, *p35S:mCherry-KLCR1* and *p35S:RFP-KLCR1* transgenes for *N. benthamiana* assays were cloned using Gateway into pB7FWG2 (Karimi *et al.*, 2002), pJOG393 (Gantner *et al.*, 2018) or pGWB455 (Nakagawa *et al.*, 2007) vectors, respectively. The mCherry- and red fluorescent protein (RFP)-tagged KLCR1 showed similar results. The *pUBQ10:RFP-TUB6* plasmid for transient expression was previously generated (Yang *et al.*, 2019). Transient expression was performed in *N. benthamiana* leaves as previously described (Grefen *et al.*, 2010). In short, *Agrobacterium tumefaciens GV3101* cells containing the desired constructs were mixed with the P19 viral suppressor (OD$_{600}$ = 0.7 for each) and incubated for 4 h (at 18°C, 200 rpm) before infiltration into the lower side of leaves from 5-wk-old plants.

Staining and quantification of mucilage area

Around 30 seeds were hydrated in water for 30 min and stained with 300 µl of 0.01% (w/v) RR (R2751; Sigma-Aldrich) for

15 min at 125 rpm in 24-well plates. After rinsing with water, the stained seeds were resuspended in 300 µl of water and imaged with a Leica M165FC stereomicroscope equipped with MC170 HD camera. The mucilage and seed projected areas were quantified using an existing ImageJ pipeline (Voiniciuc et al., 2015b).

Cellulose around hydrated seeds was stained with 0.01% (w/v) Pontamine fast scarlet 4B (S4B, also known as Direct Red 23 (212490; Sigma-Aldrich)) in 50 mM NaCl for 60 min at 125 rpm in 24-well plates (Anderson et al., 2010; Mendu et al., 2011). Alternatively, hydrated seeds were stained with 25 µg ml^{-1} Calcofluor (Megazyme C-CLFR) for 5 min, followed by three rinses with water. Seeds were imaged with a Carl Zeiss LSM 780 microscope with 10×/0.45 objective and the following excitation/emission wavelengths (S4B: 561/580–650 nm; Calcofluor: 405/410–452 nm). The lengths of cellulosic rays were measured via ImageJ.

To view surface morphology, around 30 seeds were mixed with 500 µl of 0.01% (w/v) propidium iodide for 15 min. Seeds were rinsed twice with water and imaged using a Leica LSM 900 with 10×/0.3 objective (excitation 488 nm, emission 600–650 nm).

Seed polysaccharide quantification

Nonadherent mucilage was extracted by gently mixing 5 mg seeds in water for 30 min at 125 rpm and subsequently the adherent mucilage was isolated using a ball mill (MM400; Retsch, Haan, Germany) for 30 min at 30 Hz, as previously described (Voiniciuc, 2016). The two mucilage fractions, spiked with ribose and inositol respectively, were hydrolyzed and quantified via high-performance anion exchange chromatography with pulsed amperometric detection (HPAEC-PAD), as described by Voiniciuc & Günl (2016) with the following changes. HPAEC-PAD was performed on a Metrohm 940 Professional IC Vario, using Metrosep Carb 2-250/4.0 columns and a published gradient (Mielke et al., 2021). Peaks were integrated and calibrated (manually corrected if necessary) in the MagIC Net 3.2 software (Metrohm, Herisau, Switzerland).

Crystalline cellulose was quantified using the Updegraff reagent (Updegraff, 1969) and the anthrone colorimetric assay (Foster et al., 2010), as previously adapted for Arabidopsis whole seeds (Voiniciuc et al., 2015b).

Salt stress treatments

Germination assays were performed in 24-well culture plates as described previously (Yang et al., 2021). Around 35 seeds were hydrated in 500 µl of water or 150 mM CaCl$_2$ solution per well. All the seeds were vernalized for 66 h (dark, 4°C), transferred to a chamber with constant light (100–120 µmol m^{-2} s^{-1}), 22°C and 60% humidity. The seeds were imaged every 24 h with a Leica M165FC stereomicroscope and defined as germinated when the radicle length was > 70 µm.

For the seedling salt stress assay, the seeds were placed on ½ Murashige and Skoog (½MS) agar plates, stratified for 66 h (dark, 4°C) and grown vertically in the climate-controlled chamber described above. Five-day-old seedlings of similar size were

transferred to fresh agar plates with or without 100 mM NaCl and growth was imaged using a Nikon D5600 digital camera.

Stem cell wall analyses

Stem sections were cut by hand from the basal third of stems of 6-wk-old plants and were stained in 0.01% toluidine blue O (T3260; Sigma-Aldrich) for 2 min. Stained sections were rinsed twice with water and imaged on an Axioplan 2 with AxioVision software (Zeiss).

The bottom 7 cm of mature stems was harvested and homogenized using a ball mill (MM400; Retsch) for 10 min at 30 Hz. The alcohol-insoluble residue (AIR) was extracted by sequential washes with 1 ml of 70% (v/v) ethanol, 1 ml of 1 : 1 (v/v) chloroform : methanol and 1 ml of acetone. Stem AIR was hydrolyzed and quantified via HPAEC-PAD exactly as described for seed mucilage, using ribose as the internal standard.

Confocal microscopy and image analysis

For fluorescence colocalization assays in N. benthamiana, leaf disks at 3 d post-infiltration were imaged with a Zeiss LSM880 inverted confocal microscope using a 40×/1.2 water-immersion objective. For oryzalin treatment, small pieces of transfected leaf were immersed with 1% (v/v) dimethylsulfoxide (DMSO) as mock treatment or 1% (v/v) DMSO containing 0.1 mM oryzalin (Sigma-Aldrich) for 4 h.

For the fluorescence imaging of Arabidopsis SCE cells, seeds were carefully dissected from siliques at specific stages and were imaged using a Zeiss LSM880 in Airyscan mode with a 40×/1.2 water-immersion objective. Clear images of MT linear signals were acquired using a Zeiss LSM900 with an optimized setting (40×/1.20 water-immersion objective, 4× averaging, 0.32 µm interval in Z-stack, RFP with 561 nm excitation and 575–617 nm emission). For PM, 7 DPA (days post-anthesis) seeds were prestained in 50 µM FM4-64 for 30 min before imaging. The subcellular localization of GFP-CESA3 was detected using a 63×/1.4 oil-immersion (LSM880) or 63×/1.20 water-immersion (LSM900) objective and Airyscan mode, with 330 ms exposure time based on previously described protocols (Vellosillo et al., 2015; Duncombe et al., 2020). As controls, epidermal cells of silique walls at 7 DPA were examined without dissection and seed removal. Unless stated otherwise, the time-lapse series were acquired every 5 s for 5 min. All the samples were mounted on confocal dishes with spacers (734-2905; VWR International GmbH, Dresden, Germany) and were examined with the following excitation/emission settings: green fluorescent protein (GFP; 488/505–530 nm), RFP/mCherry (514/580–635 nm), FM4-64 (514/600–700 nm).

For hypocotyl imaging, seeds were sown on ½MS agar plates and stratified for 66 h (dark, 4°C). The plates were exposed to light for 6 h at room temperature and then were wrapped with aluminum foil to keep the plates in the dark at room temperature. For the observation of RFP-TUB6 in the hypocotyl epidermal cells, the inner face of epidermal cells in zone 1 of 4-d-old dark-grown seedlings was examined as described previously (Crowell et al., 2011).

All images were processed uniformly using IMAGEJ. The maximum projection of the Z-stack or time-lapse view was generated by frames using the Z Project tool and average intensity. For evaluation of colocalization, intensity plot analysis was done via the 'RGB PROFILE PLOT' plugin. The Pearson correlation coefficient of the region of interest (ROI) from a single frame was quantified with 'COLOC 2'. Kymograph analysis of proteins and velocity quantification of GFP-CESA3 were performed as previously described (Vellosillo *et al.*, 2015). Briefly, the time-lapse stack was generated with the 'WALKING AVERAGE' plugin. The GFP-CESA3 track was depicted using a segmented line on time average image and transferred to a time-lapse stack. The kymographs were generated using the 'MULTIPLEKYMOGRAPH' plugin, and the slope of each line was used to calculate the particle velocity.

Protein–protein interactions

For coimmunoprecipitation (co-IP), proteins were extracted from transiently transformed *N. benthamiana* leaves using 1 ml lysis buffer (20 mM HEPES, pH 7.5, 40 mM KCl, 1 mM EDTA, 0.1% (v/v) Triton X-100, 1× protease inhibitor cocktail, 1 mM phenylmethylsulfonyl fluoride and 10% (v/v) glycerol; Ganguly *et al.*, 2020). Homogenate from 500 mg of plant material was centrifuged twice at 4°C at 15 000 *g* for 10 min, and 900 µl of the supernatant was incubated with 20 µl GFP-Traps or RFP-Traps (Chromotek, Planegg, Germany) overnight at 4°C on a rocking shaker. Beads were equilibrated following the manufacturer's manual using lysis buffer, without Triton-X. The next day, beads were washed four times and were boiled in 80 µl 2× Laemmli Buffer. For each sample, 40 µl was loaded on an SDS gel and blotted afterwards for 1 h. For protein detection, a 1 : 1000 dilution of the GFP antibody 3H9 (Chromotek) or the RFP antibody 6G6 (Chromotek) was used. Antimouse (1 : 20 000; Sigma A9044) and anti-rat (1 : 3000; Thermo 31470) secondary antibodies conjugated to horseradish peroxidase were used to detect RFP and GFP signals, respectively. Western blot images were acquired with a FluorChem system, using a 1 : 1 mixture of Amersham ECL-Prime and ECL-Select as chemiluminescent detection reagents.

For yeast two-hybrid assays, *IQD9* and *KLCR1* coding sequences were mobilized into pDEST32 and pDEST22 (Thermo Fisher), respectively, to generate fusion constructs with the GAL4 DNA binding domain (DBD) and GAL4 activation domain (AD). These plasmids were cotransformed in yeast cells (*Saccharomyces cerevisiae* strain pJ69-4a), as previously described (Kim *et al.*, 1997). As negative controls, GAL4 DBD and/or AD alone were included. Yeast cultures were preselected on vector-selective media (–Leu/–Trp) and interaction was estimated based on growth of yeast colonies 3 d after spotting on interaction-selective media (–Leu/–Trp/–His) supplemented with 2.5 mM 3-aminotriazole (3-AT).

Results

IQD9 and *KLCR1* control seed mucilage architecture

We hypothesized that one or more *IQD* genes are involved in Arabidopsis seed mucilage biosynthesis and screened their expression profiles using published transcriptional datasets. *IQD9* (At2G33990) and *IQD10* (At3G15050), its closest paralog, were upregulated in the seed coat at the stages of mucilage biosynthesis (Fig. 1a; Winter *et al.*, 2007; Le *et al.*, 2010). T-DNA insertions in these genes disrupted their transcription (Fig. 1b) and were screened for seed mucilage defects. While *iqd10* mutant seeds resembled the WT, two independent *iqd9* mutants displayed compact RR-stained mucilage capsules (Fig. 1c). Consistent with microarray data and the seed mucilage defects (Fig. 1), *promoter*:GUS reporter assays only showed high seed coat activity for *pIQD9* (Supporting Information Fig. S1). For *pIQD9*:GUS, the signal was strong in the maturing seed coat, as well as in flower buds and siliques. *IQD9* and *IQD10* displayed partially overlapping expression profiles, particularly in the root and shoot vasculature of 10-d-old seedlings, but shared only 47% amino acid identity (Fig. S1). Furthermore, *iqd9-1 iqd10-1* (*i9 i10*) double mutant seeds showed compact mucilage capsules resembling the *iqd9* single mutants (Fig. 1c).

Since IQD–KLCR interactions have been reported (Bürstenbinder *et al.*, 2013), we also assessed if *KLCR1/CMU1* (At4g10840) and *KLCR2/CMU2* (At3g27960) are involved in mucilage biosynthesis. *KLCR1* was highly expressed throughout seed development, while *KLCR2* transcription peaked at the preglobular and globular stages, before mucilage biosynthesis (Fig. S2a). Two knockout *klcr1* alleles, *klcr1-1* and *cmu1* (Fig. S2b; Table S1), resembled the *iqd9* compact mucilage defect (Fig. 1a), while *klcr2* seeds displayed WT-like mucilage. Both *iqd9* and *klcr1* mutants reduced mucilage capsule area by 30–40% compared to the WT (Fig. 1d), without altering seed size. The double mutant *i9 i10* and *klcr1-1 klcr2-2* (*k1 k2*) phenocopied the mucilage structure of *iqd9-1* and *klcr1-1* respectively, indicating no functional redundancy between the related genes. Transgene complementation of *i9 i10* with *IQD9* and of *klcr1-1* with *KLCR1* fully rescued the compact mucilage defects (Fig. 1). Both *iqd9* and *klcr1* mutants resembled the mucilage phenotype of *trm4*, which has SCE cells with disorganized MTs (Yang *et al.*, 2019). Moreover, *iqd9 klcr1* and *iqd9 trm4* double mutants displayed compact RR-stained mucilage capsules equivalent to the single mutants (Fig. S2c–f).

IQD9 and *KLCR1* are specifically required for cellulose distribution in mucilage

Monosaccharide analysis of nonadherent and adherent mucilage fractions revealed that the *iqd9*, *klcr1* and *trm4* mutants did not alter the content or adherence of matrix polysaccharides to the seed surface (Fig. 1e). Surprisingly, despite no impact on RR staining, the *iqd10-1* mutation correlated with a small but statistically significant reduction in total extractable monosaccharides (Fig. 1c–e). The *iqd10-1* mutation decreased rhamnose (Rha) and galacturonic acid (GalA) content in nonadherent mucilage, along with galactose (Gal) and arabinose (Ara) in adherent mucilage (Fig. 2). Nevertheless, compared to the galactoglucomannan-deficient *muci10* mutant with compact mucilage, all the MT-related mutant seeds released relatively normal levels of mucilage glycans (Fig. 2).
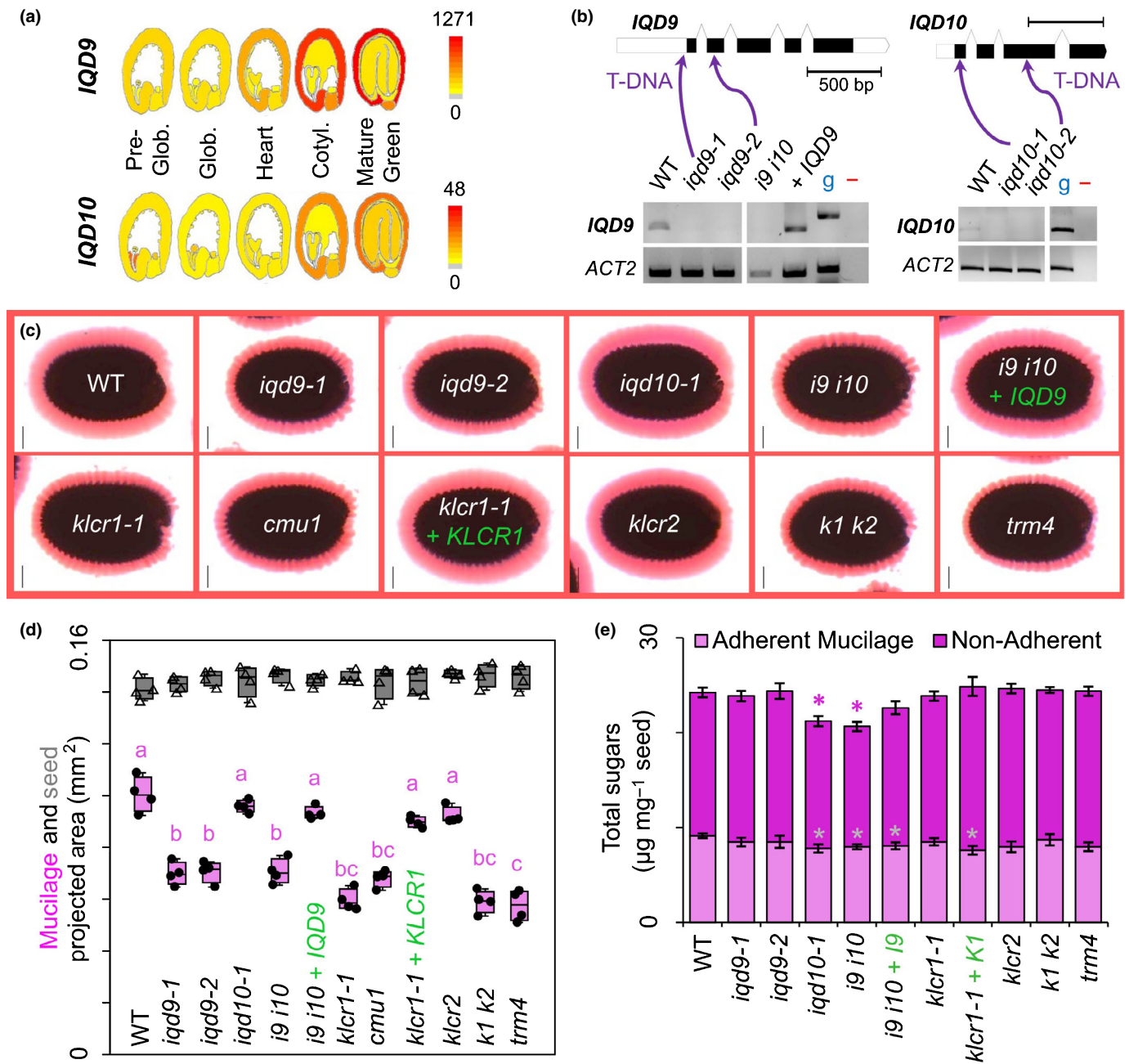
Fig. 1 Mutation of *IQD9* and *KLCR1* caused compact mucilage capsule. (a) Expression profiles during seed development (Winter *et al.*, 2007; Le *et al.*, 2010), including absolute expression values. Glob., globular; Cotyl., cotyledon. (b) Untranslated region (white bars), intron and exon (black bars) structure of candidate genes. The positions of T-DNA insertions (marked by purple arrows) and their transcriptional effects were verified using RT-PCR, *ACTIN2* as a reference gene, *g* as genomic DNA control, and − as no DNA control. Complemented transgenes are marked by + *IQD* or + *KLCR*. Bars for gene models, 500 bp. (c) Ruthenium red (RR) staining of adherent mucilage capsules after gentle shaking in water. Bars, 100 μm. (d) Seed (triangles) and RR-stained mucilage (black dots) area of four biological replicates (>20 seeds each) per genotype. Boxes show the 25–75% quartiles, the median value (inner horizontal line) and whiskers extending to the largest/smallest values. Different letters mark $P < 0.01$ for one-way ANOVA with the Tukey test. (e) Absolute amounts of monosaccharides in sequentially extracted mucilage fractions. Data show mean ± SD of five biological replicates, and asterisks mark significant changes compared to the WT (Student's *t*-test, $P < 0.001$). See Fig. 2 for detailed composition.

Since the matrix polysaccharide composition could not account for the compact mucilage defects of *iqd9* and *klcr1*, we then examined the structure of cellulose using S4B, a specific fluorescent dye (Anderson *et al.*, 2010). The *iqd9* and *klcr1* mutant seeds extruded less cellulose upon hydration (Fig. 3a) and had c. 30% shorter rays atop each columella compared with the WT

(Fig. 3b). Moreover, the mutant seeds lacked the diffuse cellulose staining that was observed between the WT rays. The S4B-stained seeds of *i9 i10* and *k1 k2* resembled the *iqd9* and *klcr1* single mutants, while *iqd10* and *klcr2* had WT-like seeds. The cellulose defects of *i9 i10* and *klcr1* mutants were rescued by *IQD9* and *KLCR1* transgene complementation, respectively,
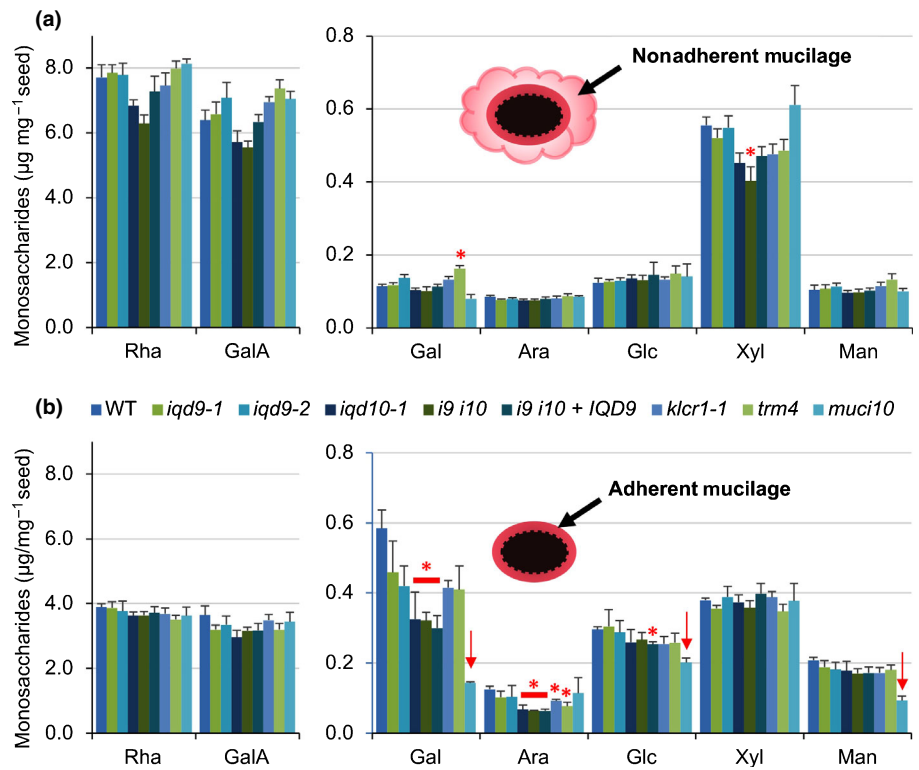
Fig. 2 Composition of matrix polysaccharides in seed mucilage extracts. (a) Nonadherent and (b) adherent mucilage polysaccharides were sequentially extracted using water and different mixing intensities. Data show mean ± SD of five biological replicates (only three for *muci10*). Red asterisks and arrows (for galactoglucomannan subunits) mark differences from the WT (Student's *t*-test, $P < 0.0001$). Monosaccharide abbreviations: Rha, rhamnose; GalA, galacturonic acid; Gal, galactose; Ara, arabinose; Glc, glucose; Xyl, xylose; Man, mannose.

using their native promoters (Fig. 3a). Using either S4B or cal-cofluor staining, *iqd9 klcr1* and *iqd9 trm4* double mutants showed similar defects in cellulose distribution to the respective single mutants (Fig. S3). While these MT-related mutants did not alter the crystalline cellulose content of whole seeds (Fig. 3c), the shorter cellulosic rays of *iqd9*, *klcr1* and *trm4* mutants also showed irregular patterns such as frayed ends (Fig. 3d). However, mutations in *IQD9* or *KLCR1* did not significantly alter SCE cell surface morphology (Fig. S4a), SCE cell area (Fig. S4b), seed ger-mination rate (Fig. S5a) or seedling sensitivity to salt (Fig. S5b). Therefore, like *TRM4* (Yang *et al.*, 2019), the expression of *IQD9* and *KLCR1* in seeds was primarily required for the archi-tecture of cellulose in mucilage.

IQD9 and IQD10 are also expressed beyond the seed coat

Based on *promoter:*GUS reporter fusions, *pIQD9* and *pIQD10* promoters were active in multiple plant tissues, including the vas-culature system (shoot and roots), developing flowers and siliques (Fig. S1). Except for anthers, *pIQD9* showed higher activity than *pIQD10* in reproductive organs and seeds (Fig. S2). *IQD10* was most highly expressed in Arabidopsis stems, and its ortholog in *Populus deltoides* (*PdIQD10*) affects the development of the woody stem (Badmi *et al.*, 2018). However, stem cross-sections of the *iqd10* single mutants and the *i9 i10* double mutant did not show the *irregular xylem* (*irx*) phenotype observed in sec-ondary cell wall mutants such as *irx14* (Fig. S6a). Furthermore, *iqd* stems had normal monosaccharide composition (Fig. S6b), while *irx14* stems were xylan-deficient, as previously described (Brown *et al.*, 2007). *IQD9* and *IQD10* are thus not

indispensable for the formation of xylem cells with thick sec-ondary cell walls, or their functions could be masked by other IQDs.

IQD9 proteins associate with MTs and interact with KLCR1

To determine the subcellular localization of IQD9 proteins, we first coexpressed IQD9-GFP fusion proteins and the MT marker RFP-TUB6 in *N. benthamiana* leaf epidermal cells. IQD9-GFP localized in striated arrays that overlapped with RFP-TUB6 at the cell cortex (Fig. S7a–c), and could be abolished by treating cells with MT-depolymerizing oryzalin. Next, we coexpressed IQD9-GFP with mCherry-tagged KLCR1 (mCherry-KLCR1) in *N. benthamiana* and found that they were colocalized in arrays resembling MTs (Fig. 4a–c). The overexpression of RFP-tagged KLCR1 alone in this plant system results in a cytosolic fluores-cence pattern (Fig. 4b), as previously reported (Bürstenbinder *et al.*, 2013; Zang *et al.*, 2021). This observation is consistent with the hypothesis that IQD proteins may function as scaffolds for the recruitment of binding partners to MTs. IQD9 and KLCR1 still colocalized when their striated patterns were disas-sembled by oryzalin treatment (Fig. 4c–e). We then tested if IQD9-GFP and RFP-tagged KLCR1 (RFP-KLCR1) interact using a bidirectional co-IP strategy following *N. benthamiana* expression. Western blotting showed that all recombinant pro-teins were present in the input fractions (Fig. S7d), before the addition of the GFP-binding beads. When proteins were purified using GFP-trap beads, RFP-KLCR1 proteins were detected on the beads only when coexpressed with IQD9-GFP, but not with
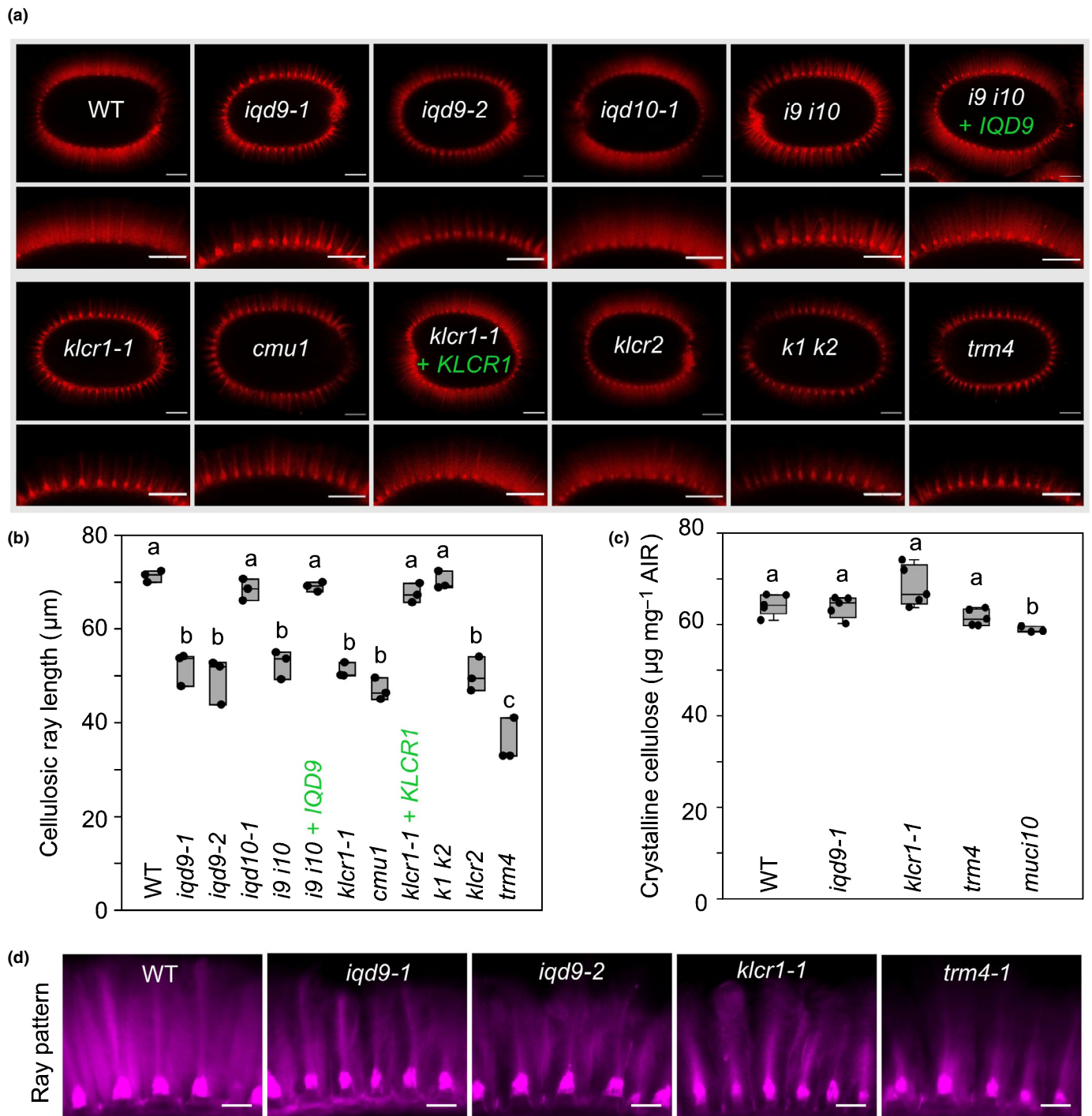
Fig. 3 IQD9 and KLCR1 are important for cellulose deposition around the seed surface. (a) S4B-stained cellulosic rays in mucilage capsules. (b) The length of cellulosic rays stained with S4B. Boxes show the 25–75% quartiles, the median value (inner horizontal line) and whiskers extending to the largest/smallest values (≥10 measurements per biological replicate). (c) Crystalline cellulose content in whole seeds (five biological replicates per genotype, except three for muci10). Different letters in (b, c) mark significant changes (one-way ANOVA with Tukey test, $P < 0.01$). (d) Representative high-magnification confocal micrographs of S4B-stained ray pattern from a separate experiment, showing irregular structures in the iqd9, klcr1 and trm4 mutants. Bars: (a) 100 μm, 20 μm (d).

GFP alone (Fig. S7d). To complement the interaction observed using GFP-based IP, we expressed the proteins in *N. benthamiana* again but pulled-down RFP-KLCR1 protein using RFP-trap beads. Only GFP-IQD9 precipitated together with KLCR1 proteins, while the GFP tag alone was not detected in the co-IP fraction (Fig. 4f). Furthermore, a yeast two-hybrid assay using GAL4 DBD and AD transcriptional domain fusions showed that IQD9 and KLCR1 proteins can directly interact (Fig. 4g). These results indicate that IQD9 proteins physically interacted with KLCR1 and were closely associated with cortical MTs in plants.

Fig. 4 IQD9 coaligns and interacts with KLCR1. (a) IQD9-GFP localized in cortical arrays in *Nicotiana benthamiana* cells. (b) RFP-KLCR1 shows diffuse localization when overexpressed on its own in tobacco. (c) Subcellular colocalization of IQD9-GFP and mCherry-KLCR1 in the mock and oryzalin-treated tobacco epidermal cells. Both transiently expressed proteins were oryzalin-sensitive. (d) Fluorescence intensity plot along the dashed line in (c). Bar, 10 μm. (e) Pearson correlation coefficient between IQD9-GFP and mCherry-KLCR1 in (c), with bars representing mean ± SD (*n* = 5 cells from five independent treatments). (f) Immunoprecipitation (IP) of proteins transiently expressed in tobacco leaves. Colored triangles marked the expected size of each protein. Labels: input (total protein supernatant) before adding the RFP-Trap beads for IP of KLCR1 proteins. (g) Yeast two-hybrid assays using DBD and AD transcriptional domains alone or fused to IQD9 and KLCR1, respectively. Only IQD9 and KLCR1 interact under the selective conditions.
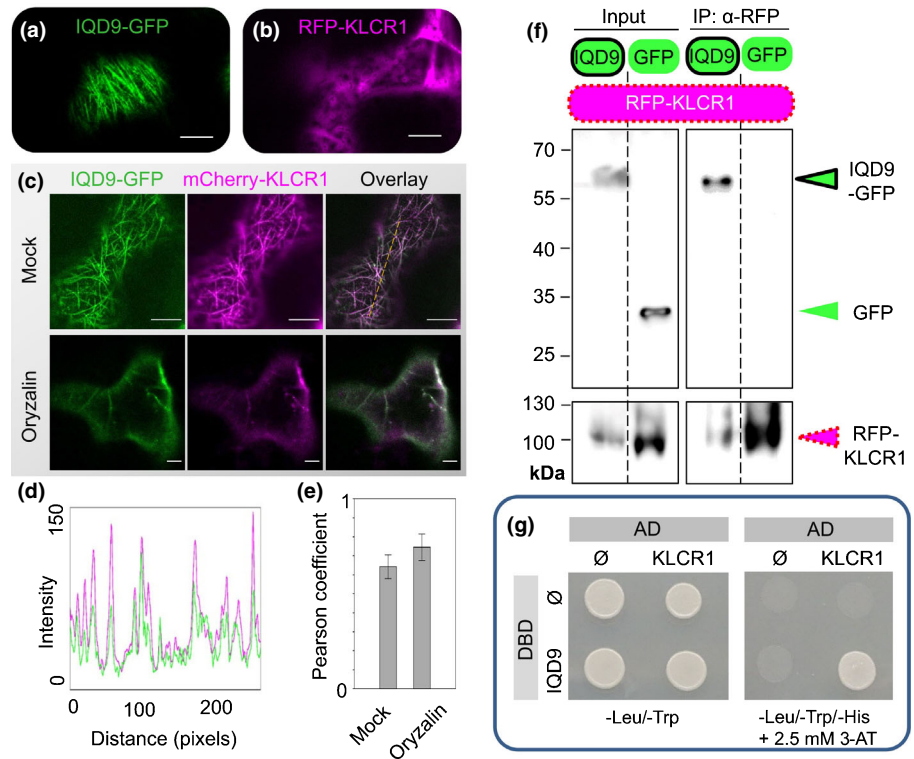
Localization of IQD9-GFP during mucilage biosynthesis

To investigate the distribution of IQD9-GFP in Arabidopsis, we examined its subcellular localization under the control of its native promoter in the complemented *iqd9* line, which rescued the mucilage defects (Fig. 1). While undetectable in young seedlings, IQD9-GFP fluorescence was evident during seed coat development (Fig. S8a), particularly at the peak stage of mucilage biosynthesis. Z-stack maximum projections revealed IQD9-GFP proteins in MT arrays, near the PM and inside the nucleus (Fig. 5a). IQD9-GFP displayed circular arrays around the cytoplasmic column, resembling previously described CESA trajectories during mucilage production (Griffiths *et al.*, 2015). At SCE cell boundaries, IQD9-GFP proteins colocalized with the PM stained by FM4-64. Time-lapse imaging revealed that IQD9-GFP proteins were static (vertical lines in the kymograph; Fig. 5b), as previously noted for KLCR/CMU proteins (Liu *et al.*, 2016). Highly immobile KLCR1-GFP proteins, expressed under its native promoter in the complemented *klcr1* line, were also associated with both MTs and PM throughout SCE development (Fig. S8b), but lacked the nuclear localization observed for IQD9-GFP. In cross-sectional views of live SCE cells, both IQD9-GFP and KLCR1-GFP were localized primarily as striated arrays adjacent to the mucilage pocket (Fig. 5c,d).

IQD9 maintains MT organization in SCE cells

Proper MT organization is essential for the establishment of mucilage architecture. The MT marker RFP-TUB6, which was selected because it was previously shown to form circular arrays around the cytoplasmic column of SCE cells at 7 DPA (Griffiths *et al.*, 2015; Yang *et al.*, 2019), was introduced into the *iqd9-1* mutant by crossing. A thick band of RFP-TUB6 arrays encircled the central cytoplasmic column of each SCE cell in the WT background, but this circular structure could not be detected in any of the examined *iqd9* SCE cells (Fig. S9). While RFP-TUB6 organization was severely disrupted in the seed coat, both the WT and *iqd9* displayed transversely oriented RFP-TUB6 arrays in hypocotyl epidermal cells (Fig. S10), despite some variation in fluorescence intensity. Since the fluorescence signals in these projected images were rather diffuse, we regrew our existing RFP-TUB6 marker lines and took higher quality images using a new confocal microscope (Leica LSM900) and smaller Z-steps. While cortical MT arrays marked by RFP-TUB6 could again be detected in the WT background, no clear MT arrays labeled by RFP-TUB6 signals were observed in *iqd9* SCE cells (Fig. 6a,b). However, linear MT arrays were detected in the epidermal cells of siliques from these plants (Fig. 6c), indicating that RFP-TUB6 protein expression or stability is particularly impaired in *iqd9* SCE cells. Similar to *iqd9* SCE cells, cortical MT arrays were also absent in the seed coat of *trm4* plants expressing RFP-TUB6 (Yang *et al.*, 2019). Therefore, the distribution of cortical MTs in the seed coat depends heavily on *IQD9*, while cytoskeleton organization in other tissues probably requires additional *IQDs*.

The absence of *IQD9* reduces CESA3 velocity

CESA3 is a key subunit of the CSC that polarly deposits cellulose in seed mucilage pockets (Griffiths *et al.*, 2015). Since
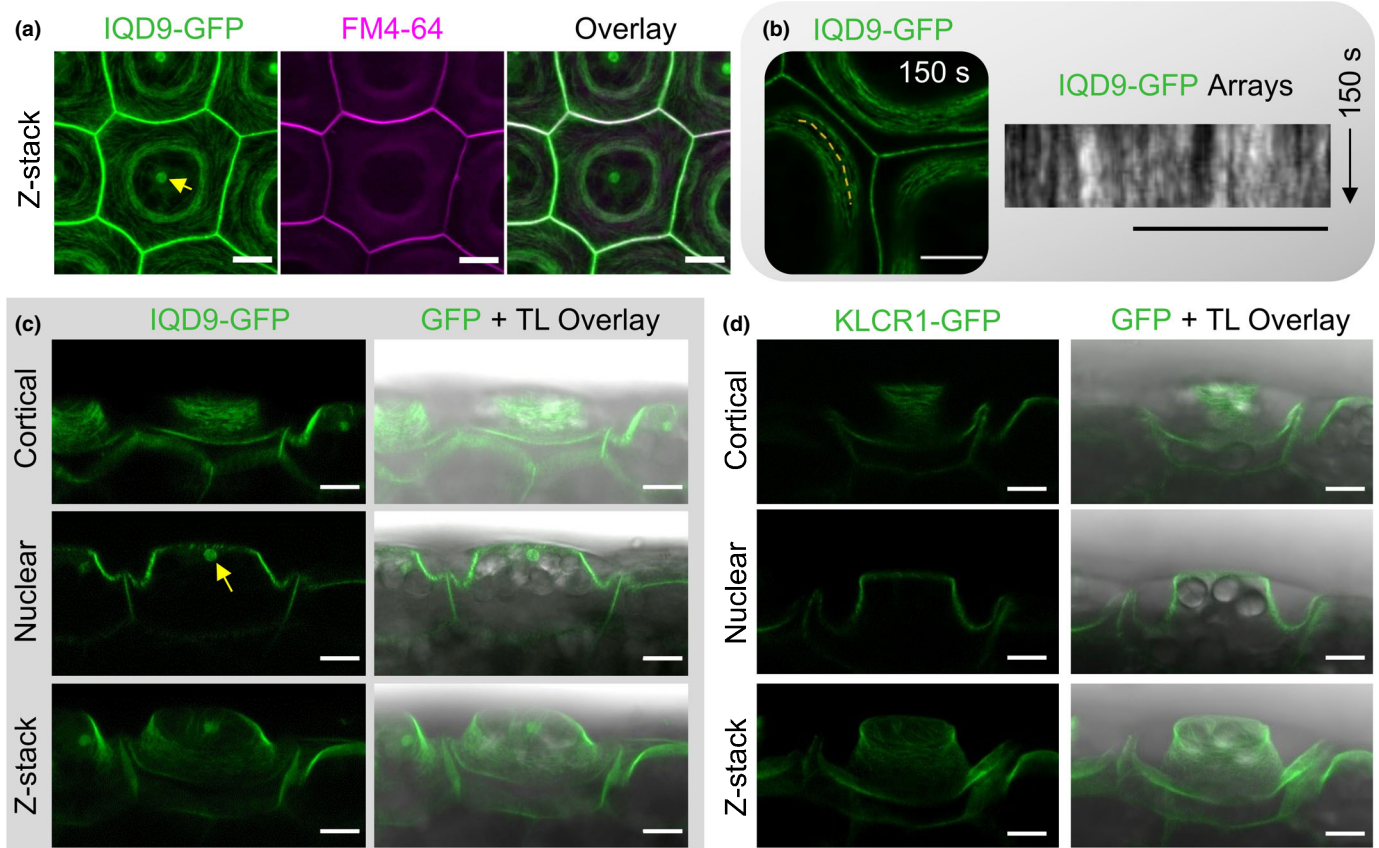
Fig. 5 IQD9 and KLCR1 localization during mucilage biosynthesis in complemented lines. (a) Z-stack maximum projection of IQD9-GFP signals in seed coat epidermal (SCE) cells stained with FM4-64 at 7 d postanthesis. IQD9 is localized at the plasma membrane, in cortical microtubule arrays and in a nuclear body (arrow). (b) Time-lapse of IQD9-GFP and kymograph along the dashed line. (c) Cross-sectional views of SCE cells expressing IQD9-GFP. The arrow marks a nuclear compartment, and the fluorescence was overlayed with transmitted light (TL) signal. (d) Cross-sectional views of SCE cells expressing KLCR1-GFP during mucilage biosynthesis. Bar, 10 μm.

cellulose distribution was disordered in *iqd9* mucilage (Fig. 3), we hypothesized that IQD9 influences CSC trajectories or motility at the cell cortex. Consistent with previous results (Griffiths *et al.*, 2015), time-lapse images revealed GFP-CESA3 proteins moved in a unidirectional, clockwise manner around the cytoplasmic column of SCE cells (Figs 7, S11). While this circular pattern of cellulose deposition was still observed for the mutant seeds (Fig. 7a), the velocity of small GFP-CESA3 particles (consistent with PM localization) decreased from 128.2 ± 29.1 nm min^{-1} in WT cells to only 83.6 ± 14.4 nm min^{-1} in *iqd9* (mean $\pm$ SD; at least 370 measurements of 16 cells from three plants per genotype; Fig. 7b, c). Consistent with their mucilage staining phenotypes (Figs 1, S2; S3), GFP-CESA3 also moved more slowly in *trm4* cells, akin to *iqd9* (Figs 7, S11). In these mutant seeds, CSC movement appeared to be uncoupled from MTs, a behavior previously described for CESA proteins in *klcr* (*cmu*) mutants (Liu *et al.*, 2016), but could not be monitored in greater detail due to the severe disruption of RFP-TUB6 localization in SCE cells (Figs 6, S9; Yang *et al.*, 2019). Taken together, IQD9 is a novel MT-associated protein that orchestrates the distribution of cellulose in seed mucilage by maintaining the

formation/stability of cytoskeletal fibers and CESA speed in SCE cells.

Discussion

In the past decade, SCE cells have become a popular model to identify and study cell wall regulators as well as carbohydrate-active enzymes. Dozens of mucilage-related genes have been gradually characterized in Arabidopsis (Voiniciuc *et al.*, 2015c; Šola *et al.*, 2019), primarily through forward and reverse genetic screens. In addition to mutants generated in the laboratory, the architecture of mucilage β-glucans was found to vary dramatically in natural populations of *A. thaliana* (Sullivan *et al.*, 2011; North *et al.*, 2014; Voiniciuc *et al.*, 2016). The Arabidopsis research findings have been accompanied by advances in the mucilage structure of food crops such as *Linum usitatissimum* (flax; Viudes *et al.*, 2020) and *Plantago ovata* (psyllium; Cowley & Burton, 2021), which contain a higher proportion of nonpectic polymers. Despite the evolution of various mucilage traits within the family Brassicaceae (Viudes *et al.*, 2021), how MTs regulate the intricate organization of this specialized secondary cell wall has remained a relatively blank slate. The Arabidopsis genome encodes hundreds
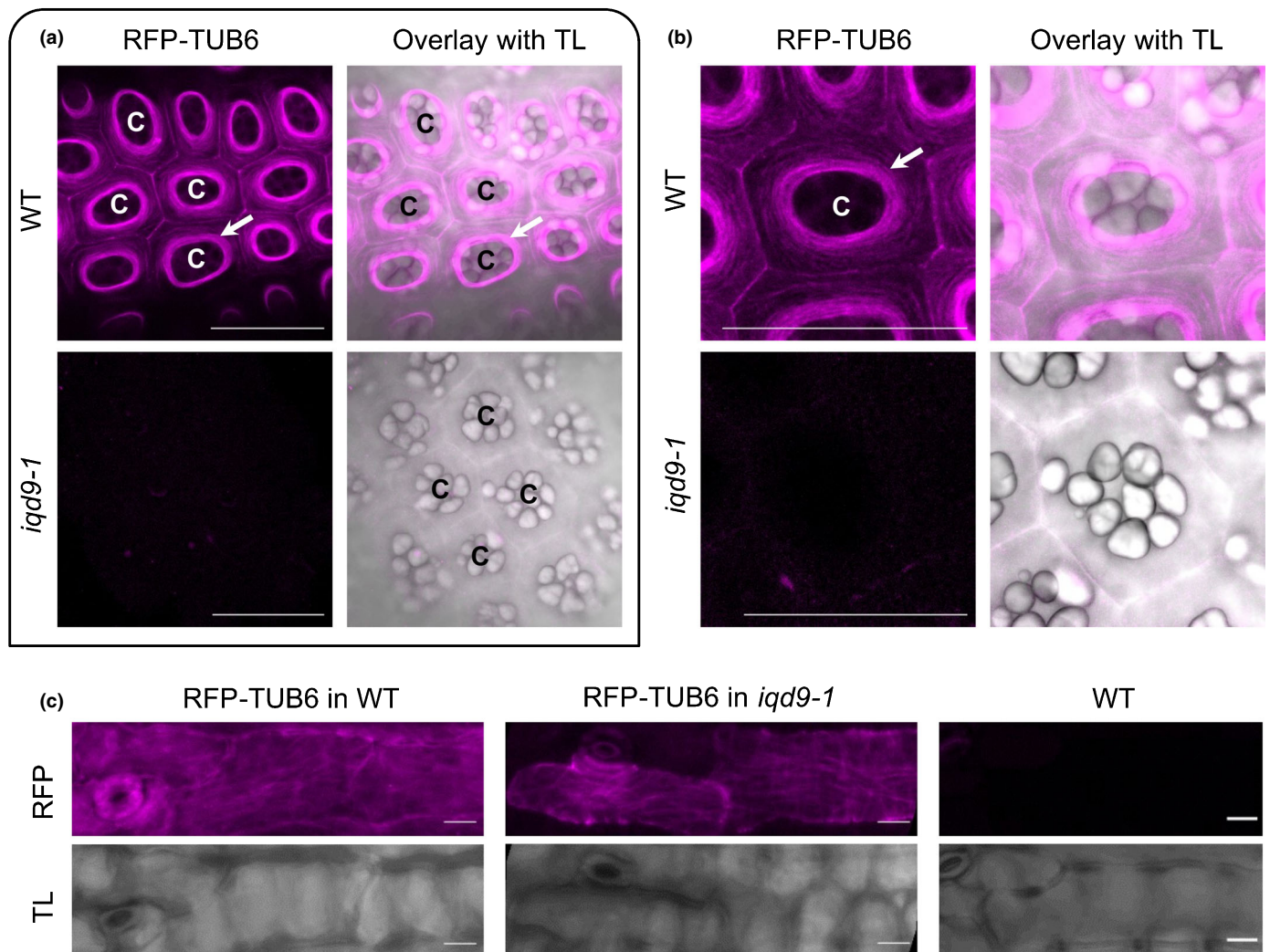
Fig. 6 RFP-TUB6 expression or stability is severely impaired in *iqd9* SCE cells. Confocal images of (a) several or (b) single seed coat epidermal (SCE) cells at 7 d postanthesis showing Z-stack maximum projections of RFP-TUB6 signals in wild-type (WT) and *iqd9-1* mutant background. Circular RFP-TUB6 arrays (arrows) encircled the cytoplasmic column (C) of WT SCE cells but were not detectable in any *iqd9-1* SCE cells. The fluorescence was also overlayed with transmitted light (TL) signals. (c) Linear microtubule arrays marked by RFP-TUB6 could be detected in the epidermal cells of both WT and *iqd9-1* silique walls, from which the seeds in (a, b) were dissected. WT without RFP-TUB6 served as a negative control. Bars: (a) 50 μm; (b, c) 10 μm.

of putative MT-associated proteins, but only MOR1 and TRM4 were previously shown to influence seed mucilage synthesis (McFarlane *et al.*, 2008; Hamada, 2014; Yang *et al.*, 2019). Additional MT-associated proteins (e.g. CSI1/POM2, CC1, IQD13 and KLCRs/CMUs) involved in cell wall biosynthesis were characterized in other tissues (Bringmann *et al.*, 2012b; Li *et al.*, 2012; Endler *et al.*, 2015; Liu *et al.*, 2016; Sugiyama *et al.*, 2017), so the players that guide mucilage biosynthesis remained unclear.

IQD9 sustains MT organization during specialized cell wall deposition

In this study, we discovered that IQD9 and its interactor KLCR1 localize to cortical arrays that resemble the circular paths of MTs (Fig. 6) and multiple CESAs (Griffiths *et al.*, 2015) during mucilage biosynthesis. IQD9 colocalized with MTs and was

sensitive to their depolymerization by oryzalin, suggesting that IQD9 may be capable of directly binding MTs like other family members. The DUF4005 domain of IQD16 was recently shown to mediate MT binding *in vivo* as well as *in vitro* (Li *et al.*, 2021). As one of the shortest family members (Abel *et al.*, 2005), IQD9 lacks the DUF4005 domain but contains a region similar to the MT2 domain of IQD13 (Fig. S1c), which is sufficient for MT localization *in vivo* (Sugiyama *et al.*, 2017). The highly immobile IQD9 proteins could function similarly to KLCR1/CMU1, its binding partner (Fig. 4), to stabilize the cortical MT arrays of SCE cells and sustain CSC speed during cellulose deposition. Consistent with this hypothesis, oryzalin treatment of SCE cells severely disrupted the trajectory and velocity of GFP-CESA3 (Griffiths *et al.*, 2015). The reduced velocity of CESA3-containing CSCs in *iqd9* and *trm4* SCE cells (Figs 7, S11) shows that multiple classes of proteins are required to shape the circular MT arrays and cellulose distribution.
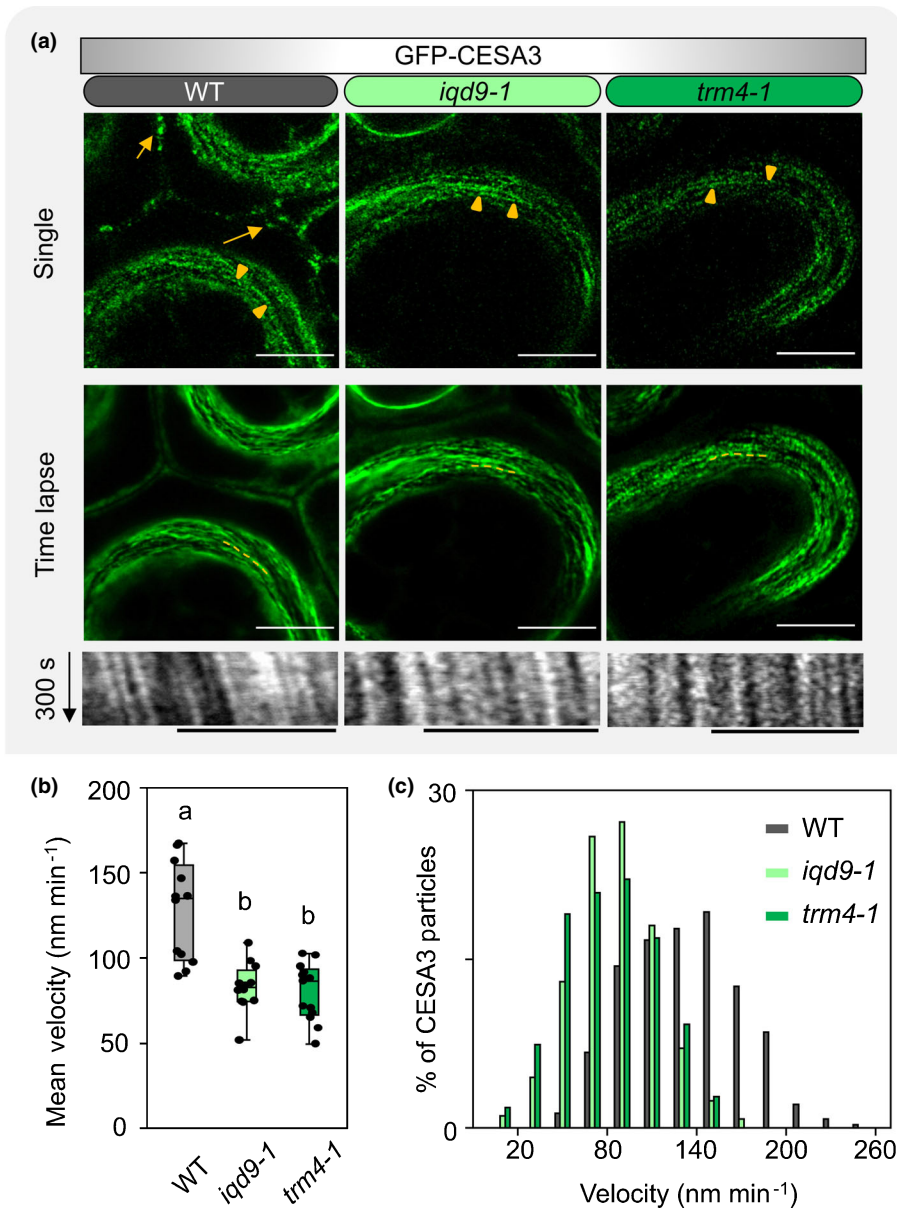
Fig. 7 The absence of *IQD9* and *TRM4* reduces GFP-CESA3 velocity. (a) Airyscan super-resolution micrographs of GFP-CESA3 in seed coat epidermal (SCE) cells at 7 d postanthesis acquired with a Leica LSM900 microscope. Arrows indicate large compartments that move much faster than the GFP-CESA3 particles in the plasma membrane and display blurring in time-lapse images. Triangles indicate cortical GFP-CESA3 with linear trajectories. The bottom row shows kymographs of GFP-CESA3 from dashed lines in the middle row. Bars, 10 µm for all, except 5 µm for kymographs. (b) Mean GFP-CESA3 velocity in 12 seeds from three plants per genotype. Boxes show 25–75% quartiles, the measurement values (dots), the median value (inner horizontal line) and whiskers extending to the largest/smallest values. Letters indicate significant differences (one-way ANOVA with Tukey test, $P < 0.01$). (c) Distribution of GFP-CESA3 velocities for the analyzed particles ($n = 390$ for WT, 378 for *iqd9-1* and 326 for *trm4-1*).

MT organization primarily affects cellulose distribution in seed mucilage

In Arabidopsis, SCE cells display MT and CSC dynamics that are considerably different from those of hypocotyl and protoxylem vessels (Griffiths *et al.*, 2015; Watanabe *et al.*, 2015; Griffiths & North, 2017), which serve as primary and secondary cell wall models. Both hypocotyl or protoxylem cells show transverse MT arrays or bundles, aligned with bidirectional movement of CSCs in the PM. The velocities of CSCs during cellulose deposition range from 200–300 nm min^{-1} in the hypocotyl to 300–400 nm min^{-1} in the protoxylem. By contrast, SCE cells display circular MT arrays around the columella, aligned with unidirectional movement of CSCs with a velocity of 80–120 nm min^{-1} (Figs 7, S11; Griffiths *et al.*, 2015). These unique MT patterns and CSC movements could lead to the polarized deposition of unusual cellulosic coils, which unwind with the expansion

of pectin polymers during Arabidopsis seed hydration (Šola *et al.*, 2019). Cytoskeletal defects in *iqd9*, *klcr1* or *trm4* mutants could slow CSC movement to result in shorter cellulose microfibrils that cannot extend to form long ray-like structures during mucilage release. The compact mucilage phenotypes of MT-related mutants and galactoglucomannan-deficient seeds such as *muci10* could be explained by similar deficiencies in the assembly of cellulose chains (Yu *et al.*, 2014; Voiniciuc *et al.*, 2015b; Griffiths & North, 2017; Yang *et al.*, 2019).

Since relatively abundant MTs line the PM of the mucilage pocket where mucilage secretion occurs (McFarlane *et al.*, 2008), MTs could also potentially target the secretion of pectin and hemicelluloses to the apoplast. However, a temperature-sensitive mutation of *MOR1* partially disrupted mucilage release without clearly affecting the secretion of vesicles to the mucilage pocket and mucilage polymer accumulation (McFarlane *et al.*, 2008). Despite the severe loss of cortical RFP-TUB6 arrays in *iqd9* and

trm4 SCE cells (Figs 6, S9; Yang *et al.*, 2019), the mutant seeds released matrix polysaccharides with WT-like amounts and composition (Fig. 2). RFP-TUB6 signals were near the detection threshold and technically challenging to visualize in *iqd9* and *trm4* seeds (Figs 6, S9; Yang *et al.*, 2019), but cortical MT arrays labeled by this fluorescent marker could be detected in *iqd9* hypocotyl (Fig. S10) and silique epidermal cells (Fig. 6c). Since the underlying reasons for the impaired accumulation or stability of RFP-TUB6 in the mutant seeds require further investigation, future studies should make use of additional MT markers tagged with brighter fluorescent protein variants (e.g. GFP) that might be better suited to study MT dynamics (such as lateral displacement; Liu *et al.*, 2016) in SCE cells. In contrast to *iqd9*, the *iqd10-1* mutation partially reduced the content of certain monosaccharides (Fig. 2) in mucilage without significantly altering the organization of polysaccharides (Figs 1, 3). Therefore, cortical MTs appear to have a relatively minor impact on the incorporation of pectin and hemicelluloses into the mucilage pockets of SCE cells. Unaltered mucilage adherence to the surface of *iqd9*, *klcr1* and *trm4* seeds is probably mediated by the presence of xylan (Voiniciuc *et al.*, 2015a; Ralet *et al.*, 2016), the SOS5 arabinogalactan protein and the receptor-like kinase FEI2 (Harpaz-Saad *et al.*, 2011; Griffiths *et al.*, 2016; Šola *et al.*, 2019).

IQD, KLCR and TRM proteins have interconnected functions

Our results and recently published findings indicate that distinct IQD proteins function in a tissue-specific manner by interacting with KLCR proteins and have potentially overlapping roles with TRM scaffolding proteins. Based on double mutant analyses (Figs S2, S3), the roles of *IQD9* in SCE cells are nearly identical to those of *KLCR1* and *TRM4*. Therefore, the encoded proteins could be associated as part of a single complex or pathway at the cell cortex. Some Arabidopsis IQDs (GFP-IQD1 or GFP-IQD2) can recruit KLCR1 to MTs when transiently coexpressed in tobacco cells (Bürstenbinder *et al.*, 2013; Zang *et al.*, 2021). The MT recruitment is consistent with our results for the transient expression of IQD9-GFP and KLCR1 (which behaves similarly when tagged with either RFP or mCherry), even though KLCR1/CMU1 alone can at least partially bind MTs (Liu *et al.*, 2016; Zang *et al.*, 2021). Furthermore, the KLCR1-IQD2 pair was recently shown to interact with the actin binding protein NET3C to modulate the shape of the endoplasmic reticulum at PM contact sites (Zang *et al.*, 2021). We hypothesize that IQD9, KLCR1 and TRM4 could be an integral part of an expanding group of proteins (Polko & Kieber, 2019) that support PM-bound CSC movement along the orientation of MT tracks. IQDs are hypothesized to function as scaffolds that recruit other proteins and may be modified by TON1/TRM/PP2A (TTP)-mediated dephosphorylation (Kumari *et al.*, 2021). Via IQ67-domain-mediated calmodulin binding (Abel *et al.*, 2005), IQDs could also participate in Ca^{2+} signaling to ultimately influence plant cell wall dynamics.

Intriguing roles of IQDs during secondary cell wall formation

Even though *IQD9* and *IQD10* promoters were active in both vegetative and reproductive organs (Fig. S1), *IQD9* was indispensable only for the organization of cellulose polymers in seed mucilage (Figs 1–3). While the expression of IQD9-GFP under its native promoter was detected only in the general seed coat (Figs 5, S4), KLCR1-GFP was expressed more ubiquitously in complemented lines. The transcription of *IQD9*, *IQD10* and *IQD13* was previously associated with secondary cell wall biosynthesis (Mutwil *et al.*, 2008). Even though we detected transcriptional activity in the vasculature (Fig. S1), the absence of *IQD9* and/or *IQD10* did not cause *irx* phenotypes found in stems with defective cellulose–hemicellulose networks (Fig. S6; Brown *et al.*, 2007). Their vascular functions could be masked by the expression of related genes such as *IQD13*, which was already shown to modulate MT organization during xylem cell formation (Sugiyama *et al.*, 2017). In poplar, the downregulation of *PdIQD10* during wood formation increased tree height, diameter and relative cellulose content (Badmi *et al.*, 2018). Since PdIQD10 interacted with PdKLCRs and could be directed to the nucleus, the elevated cellulosic biomass of the transgenic trees suggests that IQD-KLCRs participate in a tight feedback loop that regulates cellulose biosynthesis (Badmi *et al.*, 2018). In Arabidopsis, multiple *IQDs* probably have redundant roles during stem development so higher-order mutants would be needed to decipher how IQD-KLCR is involved in signaling pathways or in direct interactions with secondary wall CSCs. Unexpectedly, despite no obvious mucilage staining defects, the *iqd10-1* mutation correlated with reductions of at least 10% in rhamnogalacturonan I backbone residues and of more than 45% in Ara and Gal that are usually found in arabinogalactan proteins or pectin branches (Figs 1, 2). Based on this chemotype, the putative roles of IQD10 in the stem as well as seeds may be worthy of further investigation using additional mutant combinations.

Future avenues to tailor cellulose deposition

The localization of soluble IQD9 and KLCR1/CMU1 (Fig. 5; Liu *et al.*, 2016) proteins near or at the PM suggests that they could interact with membrane-bound CSC components, which travel in a spiral pattern during mucilage synthesis (Griffiths *et al.*, 2015). TRM4 was previously shown to maintain MT organization and directly bind CESA3 (Yang *et al.*, 2019) to enhance its mobility (Figs 7, S11). Although the mechanism that connects IQD9 and KLCR1 to TRM4 requires further investigation, we provide the first evidence that members of these three MT-associated families cooperate to direct cellulose deposition. Additional CSC-related genes are expressed during mucilage production (Griffiths & North, 2017), but their putative roles in mucilage biosynthesis remain to be investigated. Exploring the interactome of IQD9, KLCR1 and TRM4 could reveal novel targets to fine-tune the biosynthesis of cellulose, the most abundant renewable material on our planet. In addition to plant studies, the growing arsenal of proteins found to influence cellulose

biosynthesis could be rapidly expressed and engineered in surrogate hosts (Pauly *et al.*, 2019). Yeast species such as *Pichia pastoris* have already been used to express a *Populus* CESA capable of producing cellulose microfibrils *in vitro* (Purushotham *et al.*, 2016) and to identify essential protein cofactors for CESA-like enzymes that catalyze hemicellulose elongation (Voiniciuc *et al.*, 2019). Therefore, synthetic biology advances combined with attractive plant models, such as the Arabidopsis SCE cells, provide exciting avenues to refine the fibers that shape plants and many industrial products.

Acknowledgements

Author contributions

CV and KB conceived the project. BY performed most of the experiments under CV's supervision. GS and KB contributed genetic materials and performed RT-PCR, GUS and protein interaction assays. BY and CV analyzed data and wrote the manuscript with input from all authors.

ORCID

Katharina Bürstenbinder (ID) https://orcid.org/0000-0002-3493-4800
Cătălin Voiniciuc (ID) https://orcid.org/0000-0001-9105-014X
Bo Yang (ID) https://orcid.org/0000-0003-4446-0415

Data availability

The data that support the findings of this study are available from the corresponding authors upon reasonable request.

References

Abel S, Savchenko T, Levy M. 2005. Genome-wide comparative analysis of the IQD gene families in *Arabidopsis thaliana* and *Oryza sativa. BMC Evolutionary Biology* **5**: 72.

Ambrose C, Allard JF, Cytrynbaum EN, Wasteneys GO. 2011. A CLASP-modulated cell edge barrier mechanism drives cell-wide cortical microtubule organization in Arabidopsis. *Nature Communications* **2**: 430.

Anderson CT, Carroll A, Akhmetova L, Somerville C. 2010. Real-time imaging of cellulose reorientation during cell wall expansion in Arabidopsis roots. *Plant Physiology* **152**: 787–796.

Badmi R, Payyavula RS, Bali G, Guo H-B, Jawdy SS, Gunter LE, Yang X, Winkeler KA, Collins C, Rottmann WH et al. 2018. A new calmodulin-binding protein expresses in the context of secondary cell wall biosynthesis and impacts biomass properties in *Populus. Frontiers in Plant Science* **9**: 1669.

Ben-Tov D, Abraham Y, Stav S, Thompson K, Loraine A, Elbaum R, de Souza A, Pauly M, Kieber JJ, Harpaz-Saad S. 2015. COBRA-LIKE2, a member of the glycosylphosphatidylinositol-anchored COBRA-LIKE family, plays a role in cellulose deposition in Arabidopsis seed coat mucilage secretory cells. *Plant Physiology* **167**: 711–724.

Ben-Tov D, Idan-Molakandov A, Hugger A, Ben-Shlush I, Günl M, Yang B, Usadel B, Harpaz-Saad S. 2018. The role of COBRA-LIKE 2 function, as part of the complex network of interacting pathways regulating Arabidopsis seed mucilage polysaccharide matrix organization. *The Plant Journal* **94**: 497–512.

Bringmann M, Landrein B, Schudoma C, Hamant O, Hauser M-T, Persson S. 2012a. Cracking the elusive alignment hypothesis: the microtubule–cellulose synthase nexus unraveled. *Trends in Plant Science* **17**: 666–674.

Bringmann M, Li E, Sampathkumar A, Kocabek T, Hauser M-T, Persson S. 2012b. POM-POM2/CELLULOSE SYNTHASE INTERACTING1 is essential for the functional association of cellulose synthase and microtubules in *Arabidopsis. Plant Cell* **24**: 163–177.

Brown DM, Goubet F, Wong VW, Goodacre R, Stephens E, Dupree P, Turner SR. 2007. Comparison of five xylan synthesis mutants reveals new insight into the mechanisms of xylan synthesis. *The Plant Journal* **52**: 1154–1168.

Bürstenbinder K, Möller B, Plötner R, Stamm G, Hause G, Mitra D, Abel S. 2017. The IQD family of calmodulin-binding proteins links calcium signaling to microtubules, membrane subdomains, and the nucleus. *Plant Physiology* **173**: 1692–1708.

Bürstenbinder K, Savchenko T, Müller J, Adamson AW, Stamm G, Kwong R, Zipp BJ, Dinesh DC, Abel S. 2013. Arabidopsis calmodulin-binding protein IQ67-domain 1 localizes to microtubules and interacts with kinesin light chain-related protein-1. *Journal of Biological Chemistry* **288**: 1871–1882.

Cowley JM, Burton RA. 2021. The goo-d stuff: *Plantago* as a myxospermous model with modern utility. *New Phytologist* **229**: 1917–1923.

Crowell EF, Timpano H, Desprez T, Franssen-Verheijen T, Emons A-M, Höfte H, Vernhettes S. 2011. Differential regulation of cellulose orientation at the inner and outer face of epidermal cells in the *Arabidopsis* hypocotyl. *Plant Cell* **23**: 2592–2605.

Desprez T, Juraniec M, Crowell EF, Jouy H, Pochylova Z, Parcy F, Hofte H, Gonneau M, Vernhettes S. 2007. Organization of cellulose synthase complexes involved in primary cell wall synthesis in *Arabidopsis thaliana. Proceedings of the National Academy of Sciences, USA* **104**: 15572–15577.

Duncombe SG, Barnes WJ, Anderson CT. 2020. Chapter 11 – imaging the delivery and behavior of cellulose synthases in *Arabidopsis thaliana* using confocal microscopy. In: Anderson CT, Haswell ES, Dixit R, eds. *Plant cell biology. Methods in cell biology.* Cambridge, MA, USA: Academic Press, 201–213.

Endler A, Kesten C, Schneider R, Zhang Y, Ivakov A, Froehlich A, Funke N, Persson S. 2015. A mechanism for sustained cellulose synthesis during salt stress. *Cell* **162**: 1353–1364.

Foster CE, Martin TM, Pauly M. 2010. Comprehensive compositional analysis of plant cell walls (Lignocellulosic biomass) part II: carbohydrates. *Journal of Visualized Experiments* **37**: e1837.

Ganguly A, Zhu C, Chen W, Dixit R. 2020. FRA1 kinesin modulates the lateral stability of cortical microtubules through cellulose synthase-microtubule uncoupling proteins. *Plant Cell* **32**: 2508–2524.

Gantner J, Ordon J, Ilse T, Kretschmer C, Gruetzner R, Löfke C, Dagdas Y, Bürstenbinder K, Marillonnet S, Stuttmann J. 2018. Peripheral infrastructure vectors and an extended set of plant parts for the Modular Cloning system. *PLoS ONE* **13**: e0197185.

Grefen C, Chen Z, Honsbein A, Donald N, Hills A, Blatt MR. 2010. A novel motif essential for SNARE interaction with the K⁺ channel KC1 and channel gating in *Arabidopsis. Plant Cell* **22**: 3076–3092.

Griffiths JS, Crepeau M-J, Ralet M-C, Seifert GJ, North HM. 2016. Dissecting seed mucilage adherence mediated by FEI2 and SOS5. *Frontiers in Plant Science* **7**: 1–13.

Griffiths JS, North HM. 2017. Sticking to cellulose: exploiting Arabidopsis seed coat mucilage to understand cellulose biosynthesis and cell wall polysaccharide interactions. *New Phytologist* **214**: 959–966.

Griffiths JS, Šola K, Kushwaha R, Lam P, Tateno M, Young R, Voiniciuc C, Dean G, Mansfield SD, DeBolt S et al. 2015. Unidirectional movement of cellulose synthase complexes in Arabidopsis seed coat epidermal cells deposit cellulose involved in mucilage extrusion, adherence, and ray formation. *Plant Physiology* **168**: 502–520.

Griffiths JS, Tsai AYL, Xue H, Voiniciuc C, Šola K, Seifert GJ, Mansfield SD, Haughn GW. 2014. SALT-OVERLY SENSITIVE5 mediates Arabidopsis seed coat mucilage adherence and organization through pectins. *Plant Physiology* **165**: 991–1004.

Gutierrez R, Lindeboom JJ, Paredez AR, Emons AMC, Ehrhardt DW. 2009. Arabidopsis cortical microtubules position cellulose synthase delivery to the plasma membrane and interact with cellulose synthase trafficking compartments. *Nature Cell Biology* **11**: 797–806.

Hamada T. 2014. Microtubule organization and microtubule-associated proteins in plant cells. *International Review of Cell and Molecular Biology* **312**: 1–52.

Harpaz-Saad S, McFarlane HE, Xu S, Divi UK, Forward B, Western TL, Kieber JJ. 2011. Cellulose synthesis via the FEI2 RLK/SOS5 pathway and CELLULOSE SYNTHASE 5 is required for the structure of seed coat mucilage in Arabidopsis: synthesis of cellulose in seed mucilage. *The Plant Journal* **68**: 941–953.

Hu R, Li J, Wang X, Zhao X, Yang X, Tang Q, He G, Zhou G, Kong Y. 2016. Xylan synthesized by *Irregular Xylem 14* (*IRX14*) maintains the structure of seed coat mucilage in *Arabidopsis*. *Journal of Experimental Botany* **67**: 1243–1257.

Karimi M, Inzé D, Depicker A. 2002. GATEWAY vectors for Agrobacterium-mediated plant transformation. *Trends in Plant Science* **7**: 193–195.

Kim J, Harter K, Theologis A. 1997. Protein-protein interactions among the Aux/IAA proteins. *Proceedings of the National Academy of Sciences, USA* **94**: 11786–11791.

Kölling M, Kumari P, Bürstenbinder K. 2019. Calcium- and calmodulin-regulated microtubule-associated proteins as signal-integration hubs at the plasma membrane-cytoskeleton nexus. *Journal of Experimental Botany* **70**: 387–396.

Kumari P, Dahiya P, Livanos P, Zergiebel L, Kölling M, Poeschl Y, Stamm G, Hermann A, Abel S, Müller S et al. 2021. IQ67 DOMAIN proteins facilitate preprophase band formation and division-plane orientation. *Nature Plants* **7**: 739–747.

Li S, Lei L, Somerville CR, Gu Y. 2012. Cellulose synthase interactive protein 1 (CSI1) links microtubules and cellulose synthase complexes. *Proceedings of the National Academy of Sciences, USA* **109**: 185–190.

Li Y, Huang Y, Wen Y, Wang D, Liu H, Li Y, Zhao J, An L, Yu F, Liu X. 2021. The domain of unknown function 4005 (DUF4005) in an Arabidopsis IQD protein functions in microtubule binding. *Journal of Biological Chemistry* **297**: 100849.

Liang H, Zhang Y, Martinez P, Rasmussen CG, Xu T, Yang Z. 2018. The microtubule-associated protein IQ67 DOMAIN5 modulates microtubule dynamics and pavement cell shape. *Plant Physiology* **177**: 1555–1568.

Liu Z, Schneider R, Kesten C, Zhang Y, Somssich M, Zhang Y, Fernie AR, Persson S. 2016. Cellulose-microtubule uncoupling proteins prevent lateral displacement of microtubules during cellulose synthesis in Arabidopsis. *Developmental Cell* **38**: 305–315.

Lloyd C, Hussey P. 2001. Microtubule-associated proteins in plants – why we need a map. *Nature Reviews Molecular Cell Biology* **2**: 40–47.

McFarlane HE, Young RE, Wasteneys GO, Samuels AL. 2008. Cortical microtubules mark the mucilage secretion domain of the plasma membrane in Arabidopsis seed coat cells. *Planta* **227**: 1363–1375.

Mendu V, Griffiths JS, Persson S, Stork J, Downie AB, Voiniciuc C, Haughn GW, DeBolt S. 2011. Subfunctionalization of cellulose synthases in seed coat epidermal cells mediates secondary radial wall synthesis and mucilage attachment. *Plant Physiology* **157**: 441–453.

Mielke S, Zimmer M, Meena MK, Dreos R, Stellmach H, Hause B, Voiniciuc C, Gasperini D. 2021. Jasmonate biosynthesis arising from altered cell walls is prompted by turgor-driven mechanical compression. *Science Advances* **7**: eabf0356.

Mitra D, Klemm S, Kumari P, Quegwer J, Möller B, Poeschl Y, Pflug P, Stamm G, Abel S, Bürstenbinder K. 2019. Microtubule-associated protein IQ67 DOMAIN5 regulates morphogenesis of leaf pavement cells in *Arabidopsis thaliana*. *Journal of Experimental Botany* **70**: 529–543.

Mutwil M, Obro J, Willats WGT, Persson S. 2008. GeneCAT–novel webtools that combine BLAST and co-expression analyses. *Nucleic Acids Research* **36**: W320–W326.

Nakagawa T, Suzuki T, Murata S, Nakamura S, Hino T, Maeo K, Tabata R, Kawai T, Tanaka K, Niwa Y et al. 2007. Improved gateway binary vectors: high-performance vectors for creation of fusion constructs in transgenic analysis of plants. *Bioscience, Biotechnology, and Biochemistry* **71**: 2095–2100.

North HM, Berger A, Saez-Aguayo S, Ralet M-C. 2014. Understanding polysaccharide production and properties using seed coat mutants: future perspectives for the exploitation of natural variants. *Annals of Botany* **114**: 1251–1263.

Paredez AR, Somerville CR, Ehrhardt DW. 2006. Visualization of cellulose synthase demonstrates functional association with microtubules. *Science* **312**: 1491–1495.

Pauly M, Gawenda N, Wagner C, Fischbach P, Ramírez V, Axmann IM, Voiniciuc C. 2019. The suitability of orthogonal hosts to study plant cell wall biosynthesis. *Plants* **8**: 516.

Polko JK, Barnes WJ, Voiniciuc C, Doctor S, Steinwand B, Hill JL, Tien M, Pauly M, Anderson CT, Kieber JJ. 2018. SHOU4 proteins regulate trafficking of cellulose synthase complexes to the plasma membrane. *Current Biology* **28**: 3174–3182.e6.

Polko JK, Kieber JJ. 2019. The regulation of cellulose biosynthesis in plants. *Plant Cell* **31**: 282–296.

Purushotham P, Cho SH, Díaz-Moreno SM, Kumar M, Nixon BT, Bulone V, Zimmer J. 2016. A single heterologously expressed plant cellulose synthase isoform is sufficient for cellulose microfibril formation in vitro. *Proceedings of the National Academy of Sciences, USA* **113**: 11360–11365.

Ralet M-C, Crépeau M-J, Vigouroux J, Tran J, Berger A, Sallé C, Granier F, Botran L, North HM. 2016. Xylans provide the structural driving force for mucilage adhesion to the Arabidopsis seed coat. *Plant Physiology* **171**: 165–178.

Sedbrook JC, Kaloriti D. 2008. Microtubules, MAPs and plant directional cell expansion. *Trends in Plant Science* **13**: 303–310.

Šola K, Dean GH, Haughn GW. 2019. Arabidopsis seed mucilage: a specialised extracellular matrix that demonstrates the structure-function versatility of cell wall polysaccharides. *Annual Plant Reviews Online* **2**: 1085–1116.

Sugiyama Y, Wakazaki M, Toyooka K, Fukuda H, Oda Y. 2017. A novel plasma membrane-anchored protein regulates xylem cell-wall deposition through microtubule-dependent lateral inhibition of Rho GTPase domains. *Current Biology* **27**: 2522–2528.e4.

Sullivan S, Ralet M-C, Berger A, Diatloff E, Bischoff V, Gonneau M, Marion-Poll A, North HM. 2011. CESA5 is required for the synthesis of cellulose with a role in structuring the adherent mucilage of Arabidopsis seeds. *Plant Physiology* **156**: 1725–1739.

Updegraff DM. 1969. Semimicro determination of cellulose in biological materials. *Analytical Biochemistry* **32**: 420–424.

Vellosillo T, Yeats T, Sorek N. 2015. Analysis of *in vivo* cellulose biosynthesis in Arabidopsis cells by spinning disk confocal microscopy. *Bio-protocol* **5**: e1617.

Viudes S, Burlat V, Dunand C. 2020. Seed mucilage evolution: diverse molecular mechanisms generate versatile ecological functions for particular environments. *Plant, Cell & Environment* **43**: 2857–2870.

Viudes S, Dunand C, Burlat V. 2021. Myxospermy evolution in brassicaceae: a highly complex and diverse trait with Arabidopsis as an uncommon model. *Cells* **10**: 2470.

Voiniciuc C. 2016. Quantification of the mucilage detachment from Arabidopsis seeds. *Bio-Protocol* **6**: 1–9.

Voiniciuc C, Dama M, Gawenda N, Stritt F, Pauly M. 2019. Mechanistic insights from plant heteromannan synthesis in yeast. *Proceedings of the National Academy of Sciences, USA* 116: 522–527.

Voiniciuc C, Günl M, Schmidt MH-W, Usadel B. 2015a. Highly branched xylan made by IRX14 and MUCI21 links mucilage to Arabidopsis seeds. *Plant Physiology* 169: 2481–2495.

Voiniciuc C, Günl M. 2016. Analysis of monosaccharides in total mucilage extractable from Arabidopsis seeds. *Bio-Protocol* 6: e1801.

Voiniciuc C, Schmidt MH-W, Berger A, Yang B, Ebert B, Scheller HV, North HM, Usadel B, Günl M. 2015b. MUCILAGE-RELATED10 produces galactoglucomannan that maintains pectin and cellulose architecture in Arabidopsis seed mucilage. *Plant Physiology* 169: 403–420.

Voiniciuc C, Yang B, Schmidt MH-W, Günl M, Usadel B. 2015c. Starting to gel: how arabidopsis seed coat epidermal cells produce specialized secondary cell walls. *International Journal of Molecular Sciences* 16: 3452–3473.

Voiniciuc C, Zimmermann E, Schmidt MH-W, Günl M, Fu L, North HM, Usadel B. 2016. Extensive natural variation in Arabidopsis seed mucilage structure. *Frontiers in Plant Science* 7: 1–14.

Watanabe Y, Meents MJ, McDonnell LM, Barkwill S, Sampathkumar A, Cartwright HN, Demura T, Ehrhardt DW, Samuels AL, Mansfield SD. 2015. Visualization of cellulose synthases in Arabidopsis secondary cell walls. *Science* 350: 198–203.

Yang B, Hofmann F, Usadel B, Voiniciuc C. 2021. Seed hemicelluloses tailor mucilage properties and salt tolerance. *New Phytologist* 229: 1946–1954.

Yang B, Voiniciuc C, Fu L, Dieluweit S, Klose H, Usadel B. 2019. TRM4 is essential for cellulose deposition in Arabidopsis seed mucilage by maintaining cortical microtubule organization and interacting with CESA3. *New Phytologist* 221: 881–895.

Yu L, Shi D, Li J, Kong Y, Yu Y, Chai G, Hu R, Wang J, Hahn MG, Zhou G. 2014. CELLULOSE SYNTHASE-LIKE A2, a glucomannan synthase, is involved in maintaining adherent mucilage structure in arabidopsis seed. *Plant Physiology* 164: 1842–1856.

Zang J, Klemm S, Pain C, Duckney P, Bao Z, Stamm G, Kriechbaumer V, Bürstenbinder K, Hussey PJ, Wang P. 2021. A novel plant actin-microtubule bridging complex regulates cytoskeletal and ER structure at ER-PM contact sites. *Current Biology* 31: 1251–1260.

Zhang YI, Nikolovski N, Sorieul M, Vellosillo T, McFarlane HE, Dupree R, Kesten C, Schneider R, Driemeier C, Lathe R *et al.* 2016. Golgi-localized STELLO proteins regulate the assembly and trafficking of cellulose synthase complexes in Arabidopsis. *Nature Communications* 7: 11656.

Supporting Information

Additional Supporting Information may be found online in the Supporting Information section at the end of the article.

Fig. S1 *IQD9* and *IQD10* promoter activities and protein sequence alignment.

Fig. S2 *IQD9* influences mucilage deposition like *KLCR1* and *TRM4*.

Fig. S3 Staining of cellulose released from single and double mutant seeds.

Fig. S4 SCE cells and dimensions visualized with propidium iodide staining.

Fig. S5 *iqd9* and *klcr1* seeds and seedlings are not overly sensitive to salt stress.

Fig. S6 Transverse sections and monosaccharide composition of stems.

Fig. S7 IQD9 coaligns with microtubules and interacts with KLCR1.

Fig. S8 KLCR1 and IQD9 localization during SCE cell development.

Fig. S9 RFP-TUB6 localization is severely disrupted in *iqd9* SCE cells.

Fig. S10 RFP-TUB6 localizes to cortical arrays in *iqd9* hypocotyl.

Fig. S11 GFP-CESA3 moves more slowly in the *iqd9* and *trm4* seed coat.

Table S1 Mutants used in this study.

Table S2 Primers used in this study.

Please note: Wiley Blackwell are not responsible for the content or functionality of any Supporting Information supplied by the authors. Any queries (other than missing material) should be directed to the *New Phytologist* Central Office.